JOURNAL OF MATERIALS SCIENCE 23 (1988) 4357–4362

Laser glazing of an Fe–C–Sn alloy

J. G. ZHANG, X. M. ZHANG, Y. T. LIN
Shanghai Research Institute of Iron and Steel, Shanghai, China
K. JUN (T. KO)
Beijing University of Iron and Steel Technology, Beijing, China

Morphology and geometry of melted zones, cooling rates, microstructure and microhardness in the laser-glazed Fe–4%C–10%Sn alloy have been investigated. The computer simulation on the basis of the moving gaussian source model was used successfully to predict the maximum width and depth of the melted zone and the cooling rate. The microstructure from the surface to the bottom of the laser-melted zone is a non-crystalline phase, dendritic grains and a microcrystalline zone successively. Values of the average *d*-spacing of the non-crystalline phase are 0.205[6] and 0.121[9] nm, respectively; twinned martensites, having an axial ratio *c*/*a* of 1.128, existed in dendritic grains, and carbides of Fe_3C at the interdendritic regions; the microcrystalline zone was composed of α-Fe and a new bct (a = 0.415 nm, c = 0.955 nm) phase. The different microstructure in the melted zone can be explained by the results of the heat flow calculation. A fine eutectic structure (α-Fe + Fe_3C) was observed in heat-affected zones. Microhardness of the eutectic structure can be predicted by the empirical relation of fracture stress to the interlamellar spacing of pearlite.

Nomenclature

α	thermal diffusivity ($\lambda/\varrho C_p$) ($m^2 sec^{-1}$)
η	surface absorptivity (%)
λ	thermal conductivity ($W m^{-1} K^{-1}$)
ϱ	mass density ($kg m^{-3}$)
$\sigma_{f.s.}$	fracture stress ($kg mm^{-2}$)
C_p	specific heat ($J kg^{-1} K^{-1}$)
D	diffusion coefficient ($m^2 sec^{-1}$)
G	temperature gradient ($K m^{-1}$)
i, j, k	nodal point indexes in x, y and z directions, respectively
M_s	martensitic transformation temperature (K)
$n_{x_1}, n_{x_2}, n_y, n_z$	number of nodes in $-x$, x, y and z directions, respectively
P	total beam power (W)
R	solidification velocity ($m sec^{-1}$)
r	beam radius (m)
S_1	primary dendrite arm spacing (μm)
S_D	diffusional distance (m)
S_p	interlamellar spacing of pearlite (mm)
T	temperature (K)
T_0	ambient temperature (K)
t	time (sec)
v	travel speed of the specimen ($m sec^{-1}$)
x, y, z	Cartesian coordinates (m)
$\Delta x, \Delta y, \Delta z$	steps of x, y and z, respectively (m)

1. Introduction

Self-quenching using laser or electron beams is a method which can be used for production of rapidly solidified surface layers. The microstructure of these layers changed tremendously after self-quenching, i.e. refinement and homogenization of microstructure, extension of solid solubility and formation of non-equilibrium phases (non-crystalline phases and metastable crystalline phases).

Recently, the rapid solidification of Fe–C–X alloys has attracted increasing attention because of their importance in practical application. But to our knowledge of the behaviour of Fe–C–Sn alloys during rapid quenching still remains inadequate.

This paper deals mainly with the morphology and geometry of melted zones, cooling rates, microstructure and microhardness in the laser-glazed Fe–4%C–10%Sn alloy. In addition to experimental work, computer simulation was used to predict geometry of melted zones and cooling rates.

2. Mathematical model

The computer simulation on the basis of the moving gaussian source model was made of the rapid solidification in self-quenching. The input beam is stationary while the specimen moves at a constant speed, v, in the positive x direction. The heat conduction equation for a stationary coordinate system (x-y-z) is given below:

$$\varrho C_p \left(\frac{\partial T}{\partial t} + v\frac{\partial T}{\partial x}\right) = \frac{\partial}{\partial x}\left[\lambda(T)\frac{\partial T}{\partial x}\right] + \frac{\partial}{\partial y}\left[\lambda(T)\frac{\partial T}{\partial y}\right] + \frac{\partial}{\partial z}\left[\lambda(T)\frac{\partial T}{\partial z}\right] \quad (1)$$

The simplified assumptions are as follows:

1. Except during the initial and the final transients

0022–2461/88 $03.00 + .12

of the self-quenching process, the temperature distribution in a specimen of sufficient length is steady. Under such conditions the time dependent term in Equation 1 becomes zero.

2. The latent heat of phase transformation is neglected.

3. Thermal properties of the liquid and the solid are independent of temperature.

4. Cooling is by conduction only; radiation and convection are neglected.

5. The power distribution in the input beam is gaussian. Thus Equation 1 can be simplified as follows:

$$\varrho C_p v \frac{\partial T}{\partial x} = \lambda \left(\frac{\partial^2 T}{\partial x^2} + \frac{\partial^2 T}{\partial y^2} + \frac{\partial^2 T}{\partial z^2} \right) \quad (2)$$

Equation 2 is then subject to the following boundary conditions:

$$\frac{\partial T}{\partial y} = 0 \quad (y = 0) \quad (3)$$

$$T = T_0 \quad (x^2 + y^2 + z^2)^{1/2} \gg 0 \quad (4)$$

$$-\lambda \frac{\partial T}{\partial z} = \frac{P\eta}{2\pi r^2} \exp\left(-\frac{x^2 + y^2}{2r^2} \right) \quad (z = 0) \quad (5)$$

The finite difference representation of the heat conduction equation can be put in the following form:

$$\begin{aligned} T(i, j, k) = & \left\{ \frac{\alpha}{(\Delta x)^2} [T(i + 1, j, k) + T(i - 1, j, k)] \right. \\ & + \frac{\alpha}{(\Delta y)^2} [T(i, j + 1, k) + T(i, j - 1, k)] \\ & + \frac{\alpha}{(\Delta z)^2} [T(i, j, k + 1) + T(i, j, k - 1)] \\ & - \frac{v}{2(\Delta x)^2} [T(i + 1, j, k) \\ & \left. - T(i - 1, j, k)] \right\} \Big/ 2\alpha \left(\frac{1}{(\Delta x)^2} + \frac{1}{(\Delta y)^2} \right. \\ & \left. + \frac{1}{(\Delta z)^2} \right) - (n_{x_1} - 1) \leqslant i \leqslant (n_{x_2} - 1), \\ & 2 \leqslant j \leqslant (n_y - 1), \; 2 \leqslant K \leqslant (n_z - 1) \end{aligned} \quad (6)$$

Equation 6 together with the boundary conditions was used to solve the temperature distribution in the specimen. The successive over-relaxation method was employed. The computation was continued until the convergence criterion (Equation 7) was satisfied

$$|T(i, j, k)_{new} - T(i, j, k)_{old}| \leqslant 2\,(\mathrm{K}) \quad (7)$$

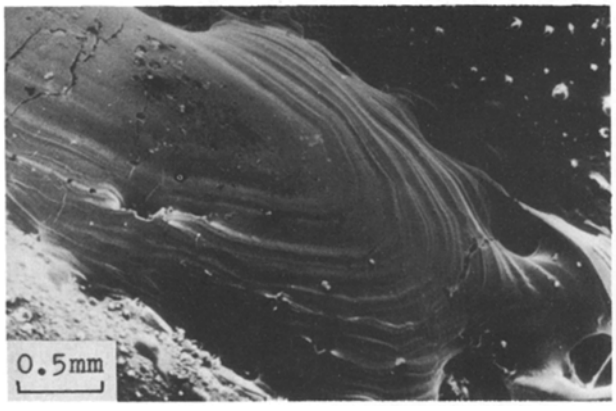

Figure 1 Morphology of the laser-glazed surface (SEM).

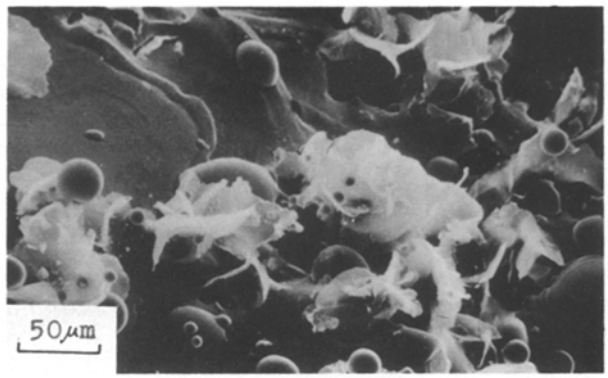

Figure 2 Appearance of flower-like graphite (SEM).

3. Experimental details

The alloy of composition (wt %) Fe–4C–10Sn was melted in vacuum and then cast into a 20 mm diameter ingot mould. Laser treatments were made with a 1.1 kW CW CO_2 laser. The traverse speed of specimens relative to the beam was 10 cm sec^{-1}. Phosphate coating was used on the top surfaces of the specimens to enhance surface absorptivity and to ensure reproducibility.

After laser glazing, the as-melted surfaces were observed by SEM. Then specimens were cross-sectioned and studied by optical metallography, X-ray diffraction, TEM and electron microprobe analysis. The metallographic specimens were prepared by electro-etching in 10% chromic acid solution using voltage of 6 V. TEM samples were obtained by ion milling. Measurements were made of the depth, width and hardness of laser-glazed regions.

4. Results and discussion

4.1. Morphology and geometry of the melted zone

Fig. 1 shows the top view of the as-melted surface observed by SEM. Ripples, cracks and small holes can be seen on the surface. SEM examination at higher magnification reveals the flower-like graphite in holes (Fig. 2). Fig. 3 shows the cross-section of the laser-glazed zone, where a "hill" is observed in the upper part of the melted zone. It seems possible that the existence of the hill, which was not observed in laser-

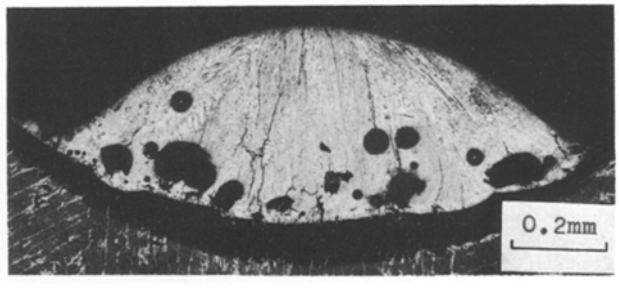

Figure 3 An optical micrograph of a cross-section of the laser-glazed zone.

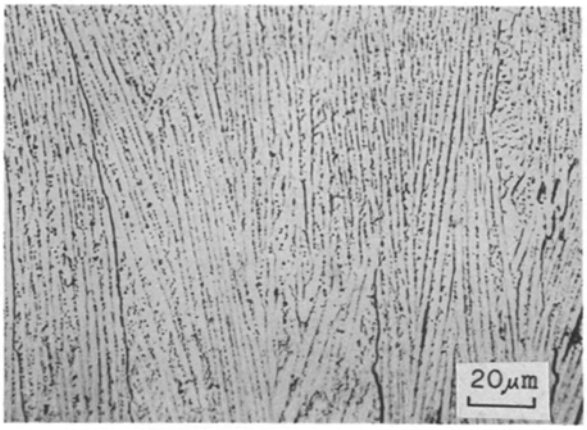

Figure 4 An optical micrograph of microstructure of the laser-glazed zone.

glazed Fe–Ge and Fe–C–Ge alloys, is associated with special physical properties of the melt of Fe–C–Sn alloys (e.g. surface tension). A heat-affected zone is observed in Fig. 3.

The measurements of the cross-sectional profile of the melted zones showed that the maximum melt width was in the range 1.22 to 1.27 mm; the maximum melt depth was 0.18 to 0.19 mm. Using the computer simulation indicated above, we predicted the width to be 1.28 mm and the depth to be 0.197 mm. The agreement is fairly good.

4.2. Cooling rate

The average dendrite arm spacing of $\sim 1.8\,\mu m$ was determined from the microstructure of laser-glazed zones shown in Fig. 4. Davies *et al.* [1] obtained the empirical relation between the cooling rate, $\partial T/\partial t$, and the primary dendrite arm spacing, S_1, for Nimonic 80A as follows

$$S_1 = 97\left(\frac{\partial T}{\partial t}\right)^{-0.36} \quad (8)$$

From Equation 8 a cooling rate of $6.5 \times 10^4\,K\,sec^{-1}$ was obtained for the spacing of $1.8\,\mu m$.

Calculating the temperature gradient $\partial T/\partial x$, from the computer simulation results, we obtained a cooling rate of $9.75 \times 10^4\,K\,sec^{-1}$ from the following formula

$$\frac{\partial T}{\partial t} = v\left(\frac{\partial T}{\partial x}\right) \quad (9)$$

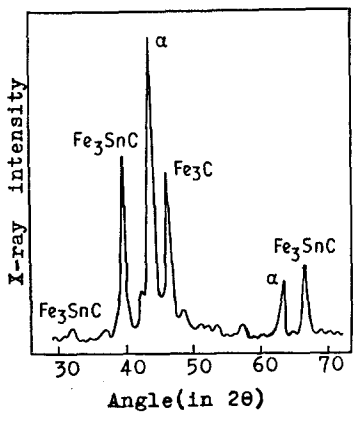

Figure 5 X-ray diffractometer traces of the alloy before laser glazing (Cu$K\alpha$ radiation).

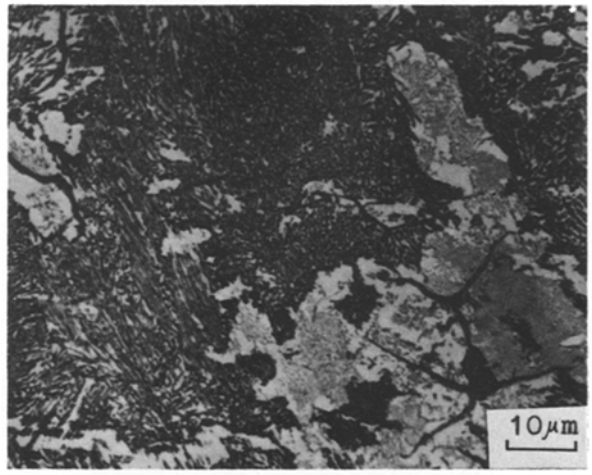

Figure 6 An optical micrograph of microstructure of the alloy before laser glazing.

Although it is only an approximation to estimate cooling rates by using empirical relation 8, it is reasonable to state that the cooling rate in the present work ranges from $\sim 5 \times 10^4$ to $\sim 1 \times 10^5\,K\,sec^{-1}$ because the values of cooling rate calculated on the basis of the mathematical model and those estimated from the microstructure are in good agreement.

4.3. Microstructure before laser glazing

Fig. 5 shows the X-ray diffraction spectrum of the alloy before laser glazing. α-Fe, Fe_3C and Fe_3SnC, which is cubic ($a = 0.3867$ nm), exist in the alloy. Jolly and Grellet [2] suggested the reaction as follows:

$$Fe_3C + FeSn \rightarrow Fe_3SnC + Fe \quad (10)$$

The microstructure before laser glazing is shown in Fig. 6, where pearlite is in light contrast, regions which contain predominantly Fe_3SnC are in dark contrast, and the thread-like black feature at the lower right-hand corner is graphite.

Electron diffraction analysis of thin foil specimens under various orientations reveals that Fe_3SnC has ordered fcc structure.

4.4. Microstructure after laser glazing

Examination of the laser-glazing specimen with an electron microprobe analyser showed fairly even distribution of each element in the laser-melted zone. The content of carbon in the zone is 3.7 wt %, which is less than the average composition of the alloy because of the existence of graphite.

Careful inspection of laser-melted zones in TEM did not reveal Fe_3SnC. This implies that Reaction 10 was suppressed by rapid solidification processing. The evidence to support this is that Polesya *et al.* [3] have not found FeSn in rapidly solidified Fe-rich Fe–Sn alloys (< 32.1 at % Sn).

In the upper part of the laser-glazed zone, regions without diffraction contrast in TEM were found: They appeared to be non-crystalline and lacking micro-structural features. The selected-area diffraction pattern from these regions illustrated in Fig. 7 exhibited diffuse rings. Table I gives values of average *d*-spacing of these diffuse rings, and also summarizes those in

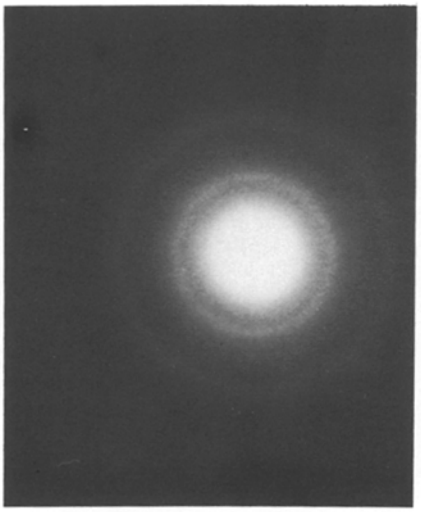

Figure 7 A selected-area diffraction pattern from the non-crystalline phase.

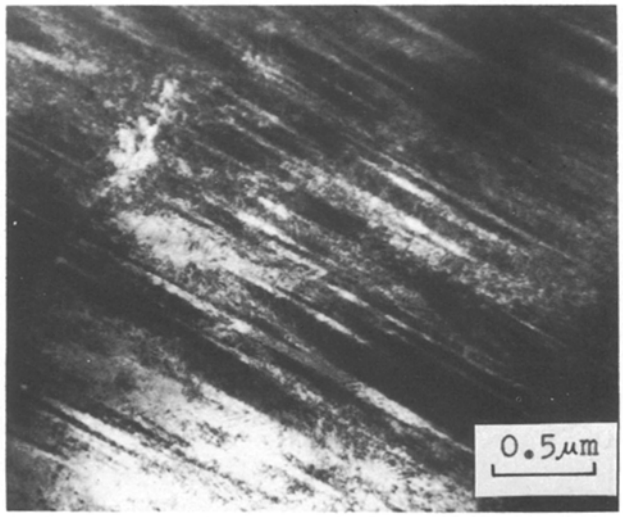

Figure 8 Twinned martensites in dendritic grains (TEM).

Fe–C–P alloys obtained by Duwez and Lin [4], in an Fe–3.8 wt % alloy by Shingu *et al.* [5], and in Fe–C–Si alloys by Sare [6] in order to make a comparison. These data lead us to assume that these non-crystalline phases in different Fe–C–X alloys are the same.

In most of the laser-glazed zone, except at the bottom of it, dendritic grains as shown in Fig. 4 appeared. TEM studies demonstrated that carbides of Fe_3C were present in interdendritic regions, and martensites, $\sim 0.1\,\mu m$ wide, which consisted of fine twins of less than 10 nm (Fig. 8), were present in dendritic grains. The electron diffraction pattern of the martensite was indexed carefully, and it yielded an axial ratio $c/a = 1.128$. Neglecting the effect of tin, we applied the relation to Fe–C alloys [7]:

$$c/a = 1.000 + 0.045\,(\text{wt}\,\%) \qquad (11)$$

From Eqaution 11 a carbon content of 2.84 wt % was obtained which was less than the average value of 3.7 wt % determined with an electron probe analyser in the laser-melted zone. This is not surprising if existence of carbides in the interdendritic regions and an error in indexing the electron diffraction patterns are considered.

As no reliable experimental data concerning the effect of tin on the martensitic transformation temperature (M_s) of iron-base alloys are available at present, the relation of the M_s temperature to the concentration of carbon in Fe–C alloy [8] is therefore used

$$M_s\,(^\circ C) = 520 - 320\,(\text{wt}\,\%\,C) \qquad (12)$$

TABLE I Average d-spacing

Alloy system	First ring d_1 (nm)	Second ring d_2 (nm)	d_1/d_2	Reference
Fe–C–Sn	0.205[6]	0.121[9]	1.68[7]	This work
Fe–C–P	0.206[7]*	0.122[6]*	1.68[6]	[4]
Fe–C	0.203	0.120	1.69[2]	[5]
Fe–C–Si	0.204	0.121	1.68[6]	[6]

*Calculated from the X-ray diffraction data obtained in the original reference.

According to Equation 12 the M_s temperature of the alloy containing 2.84 wt % carbon is significantly lower than room temperature. This suggests that the M_s temperature of the alloy is increased by rapid quenching. It is interesting to note that contradictory results of effect of cooling rates on M_s temperature have been reported in the literature: the M_s temperature has been found to be depressed by high cooling rates in Fe–Ni [9], Fe–Mn and Fe–Ni–C alloys [10], but to be increased in Fe–Mo–C alloys [11]. The theory of Donachie and Ansell [12] can be used to explain the results obtained under the present conditions: rapid quenching rates suppress the formation of large carbon atmospheres, thus weakening the austenite, which raises the M_s temperature.

It should be emphasized that tin did exist in martensites, although the effect of tin was neglected because of the lack of experimental data in the previous discussion. By using the equation $S_D = (Dt)^{1/2}$, it was found that if the diffusion of tin was considered, then the tin content in martensites at the centre of the dendrites was higher than the equilibrium value because the diffusional distance $S_D \simeq 0.22\,\mu m$ was considerably smaller than the dendrite arm spacing ($\sim 1.8\,\mu m$).

The microstructure near the bottom of the melted zone is significantly different from the above-mentioned dendritic grains. A low-magnification micrograph of a replica of this area reveals a featureless microstructure, which consists of microcrystallites of size ~ 20 nm illustrated in Fig. 9 obtained by TEM observation of thin foils at high magnification. Fig. 10 is the electron selected area diffraction pattern from the area shown in Fig. 9 confirming the existence of α-Fe and a new phase. Indexing the rings shown in Fig. 10 with a computer program, we found that the new phase had b c t structure with $a = 0.415$ nm and $c = 0.955$ nm. Dark-field TEM micrographs showed that the areal fraction occupied by the b c t phase was small.

The fact that obviously different microstructures occurred in different parts of the laser-melted zone can be interpreted by the results of heat flow calculation. In the upper part of the laser-melted zone a moderate

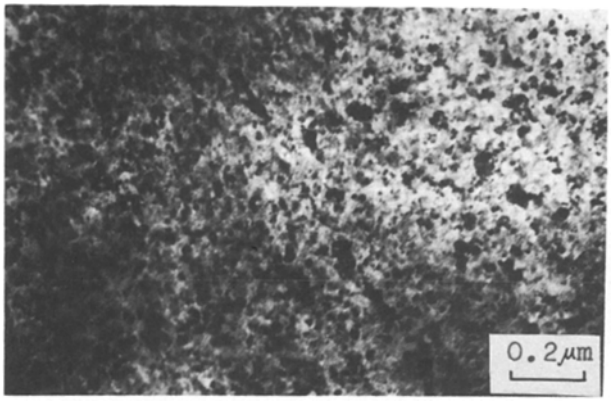

Figure 9 Microcrystalline zone (TEM).

solidification rate and a high cooling rate resulted in the formation of a non-crystalline phase. A narrow zone with the mode of plane front solidification was yielded near the bottom of the melted zone due to the large value of G/R, where G is the temperature gradient in the liquid ahead of the moving interface and R the solidification velocity. In the remaining part the value of G/R became smaller; dendritic grains therefore occurred.

In the heat-affected zone, complex eutectic structure was seen (Fig. 11). Electron diffraction analysis demonstrated that the eutectic structure was composed of α-Fe and Fe_3C. The interlamellar spacing of the eutectic structure was apparently less than that of the pearlite before laser glazing, therefore the microhardness of the former was higher than that of the latter.

4.5. Microhardness

Table II shows values of the Vickers microhardness. Except for the heat-affected zone, no appreciable hardness variation was determined by subsequent quenching into liquid nitrogen.

The empirical relation between the interlamellar spacing of pearlite, S_p, and the fracture stress, $\sigma_{f.s.}$ was given by [13]

$$\sigma_{f.s.} = 44.5 + 0.010\, S_p^{-1} \quad (13)$$

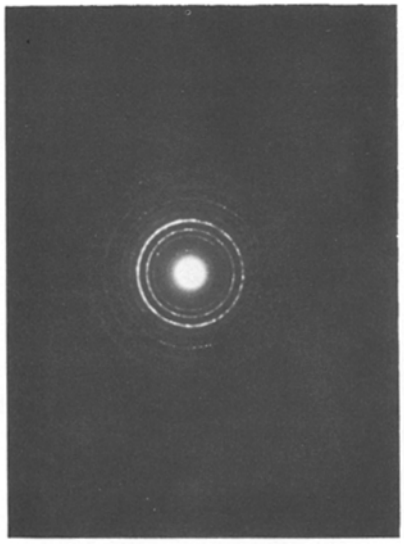

Figure 10 A selected-area diffraction pattern from the b.c.t phase.

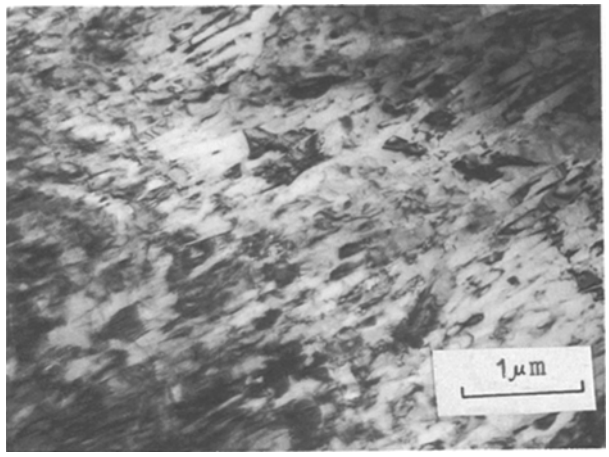

Figure 11 Eutectic structure in heat-affected zones (TEM).

Substituting the values of the fracture stress converted from the microhardness shown in Table II into Equation 13, we obtained a value of interlamellar spacing of pearlite before laser glazing of 198 nm, and that of the eutectic structure in the heat-affected zone was 38.8 nm. The values of interlamellar spacing determined from transmission electron micrographs of pearlite (not shown here) and determined from Fig. 10 were in the range 150 to 210 and 55 to 80 nm, respectively. They were in rough agreement.

Substituting the martensitic width of $\sim 0.1\,\mu m$ into the relation of the hardness of martensites to their size obtained by Duflos and Cantor [14] in terms of the Hall–Petch equation, we find that the hardness of martensites in the laser-melted zone should be $\sim 1200\,kg\,mm^{-2}$, which is significantly larger than the experimental value shown in Table II. A similar discrepancy was also found by Rayment and Cantor [15] in rapidly solidified Fe–C–W alloys. They found that it was difficult to explain why the RS and solid-state quenched hardness of FeWC 1 were so similar when the microstructure was five times finer.

It is noteworthy that there are two opposite effects of a quench rate on the hardness of martensites. On the one hand increasing a quench rate raises the hardness of martensites because of a decrease in the size of martensites, which can be interpreted in terms of a Hall–Petch effect, but on the other hand a rapid quench rate causes a decrease in martensite strength which was commonly observed [16] and can be explained by several different mechanisms. The first effect (the Hall–Petch effect) alone can satisfactorily account for the hardness of martensites in rapidly solidified pure iron as reported by Duflos and Cantor [14]. However, for Fe–C–X alloys the second effect must be also considered. It is assumed that rapid quench rates suppress carbon atmosphere formation, thus causing an increase of M_s temperature as discussed above, and a decrease of martensite strength in rapidly solidified Fe–C–X alloys.

5. Conclusions

In the laser-glazed Fe–4%C–10%Sn alloy certain interesting facts can be summarized.

1. A computer simulation on the basis of the moving gaussian source model was used to predict the

TABLE II Values of the Vickers microhardness number, VHN, at 100 g

	Before laser glazing		After laser glazing	
	Pearlite zone	Fe_3SnC zone	Laser-melted zone	Heat-affected zone
Annealed	273	649	–	–
As-melted	–	–	690	795
Liquid nitrogen quenched	270	660	685	836

maximum width and depth of melted zones and cooling rates, which were in agreement with the experimental values determined.

2. A non-crystalline phase was found in the upper part of the laser-melted zone. Values of average d-spacing of the first and second diffuse rings in the electron diffraction pattern from the non-crystalline phase are 0.205[6] and 0.121[9] nm, respectively.

3. Twinned martensites, having an axial ratio c/a of 1.128, were present in dendritic grains, which occurred in most of the laser-glazed zone except at the bottom.

4. A new phase of bct structure (a = 0.415 nm, c = 0.955 nm) has been found in the microcrystalline zone.

5. A eutectic structure consisting of α-Fe and Fe_3C was observed in the heat-affected zones. The hardness of the eutectic structure can be predicted by the empirical relation between fracture stress and the interlamellar spacing of pearlite.

6. Fe_3SnC, which was present before laser glazing, was not seen in laser-glazed zones.

Acknowledgements

The authors thank Miss L. Y. Chen for laser beam glazing the specimens, using equipment in Shanghai Institute of Optic and Fine Mechanics, Academia Sinica.

References

1. H. A. DAVIES, N. SHOHOJI and D. H. WARRINGTON, in "Proceedings of the 2nd International Conference on Rapid Solidification Processing", Reston, March 1980, edited by R. Mehrabian, B. H. Kear and M. Cohen (Claitor's, Baton Rouge, 1980) p. 153.
2. P. JOLLY and B. GRELLET, *Mem. Sci. Rev. Met.* **68** (1971) 703.
3. A. F. POLESYA and P. S. SLIPCHNKO, *Metalphysics* **51** (1974) 112.
4. P. DUWEZ and S. C. H. LIN, *J. Appl. Phys.* **38** (1967) 4096.
5. P. H. SHINGU, K. KOBAYASHI, K. SHIMOMURA and R. OZAKI, *Scripta Metall.* **8** (1974) 1317.
6. I. R. SARE, *ibid.* **9** (1975) 607.
7. C. S. ROBERTS, *Trans. AIME* **197** (1953) 203.
8. T. Y. HSU, *Acta Metall. Sinica* **15** (1979) 329.
9. Y. INOKUTI and B. CANTOR, *Scripta Metall.* **10** (1976) 655.
10. *Idem, J. Mater. Sci.* **12** (1977) 946.
11. I. R. SARE and R. W. K. HONEYCOMBE, *ibid.* **13** (1978) 1991.
12. S. J. DONACHIE and G. S. ANSELL, *Met. Trans.* **6A** (1975) 1863.
13. A. R. MARDER and B. L. BRAMFITT, *ibid.* **7A** (1976) 365.
14. F. DUFLOS and B. CANTOR, in "Proceedings of the 3rd International Conference on Rapidly Quenched Metals", Vol. I, Brighton, July 1978, edited by B. Cantor (The Metals Society, London, 1978).
15. J. J. RAYMENT and B. CANTOR, *Met. Trans.* **12A** (1981) 1557.
16. J. M. CHILTON and P. M. KELLY, *Acta Metall.* **16** (1968) 637.

Received 11 June
and accepted 27 August 1987